Schmitt, A. K., Stockli, D. F., Niedermann, S., Lovera, O. M., Hausback, B. P. (2010): Eruption ages of Las Tres Vírgenes volcano (Baja California): A tale of two helium isotopes. - Quaternary Geochronology, 5, 5, 503-511,

DOI: 10.1016/j.quageo.2010.02.004

Eruption Ages of Las Tres Vírgenes Volcano (Baja California): a Tale of Two Helium Isotopes

Revised Version Submitted to Quaternary Geochronology

Axel K. Schmitt[1,*], Daniel F. Stockli[2], Samuel Niedermann[3], Oscar M. Lovera[1], Brian P. Hausback[4]

[1]Department of Earth and Space Sciences, University of California Los Angeles, 595 Charles Young Drive E, Los Angeles, CA 90095, USA

[2]Department of Geology, University of Kansas, 120 Lindley Hall, 1475 Jayhawk Boulevard, Lawrence, KS 66045-7613, USA

[3] Helmholtz-Zentrum Potsdam – Deutsches GeoForschungsZentrum, Telegrafenberg, D-14473 Potsdam, Germany

[4]Geology Department, California State University, Sacramento, CA 95819-6043, USA

* To whom correspondence should be addressed: E-mail: axel@oro.ess.ucla.edu

Abstract

La Virgen tephra is the product of the youngest and most voluminous explosive eruption of Las Tres Vírgenes volcano (Baja California). Combined U–Th and (U–Th)/He zircon dating allows accurate correction for uranium-series disequilibrium, and yields an eruption age for La Virgen tephra of $30.7^{+1.8}_{-1.4}$ ka (2σ). ^{3}He surface exposure ages (T_3) of overlying mafic lavas are 25.5±4.4 and 22.0±2.5 ka, and agree within uncertainties with ^{21}Ne exposure ages (T_{21}). A previously undated tephra south of Las Tres Vírgenes volcano yielded U–Th and (U–Th)/He zircon ages overlapping those of La Virgen tephra, which suggests that both units are identical. T_3 and T_{21} ages for a nearby dome lava are slightly older (T_3 = 42.5±3.8 ka). No difference in eruption ages was found between samples from proximal and distal La Virgen tephra. (U–Th)/He and surface exposure ages are stratigraphically consistent, whereas a published Holocene ^{14}C charcoal age from the distal site could not be confirmed. Instead, abundant zircons with (U–Th)/He ages between ~1 and 22 Ma are interpreted as undegassed detrital grains, suggesting reworking of pumice at the distal location. The results presented here underscore the potential of combined U–Th and (U–Th)/He zircon dating for Quaternary tephrochronology.

Keywords: uranium series, zircon, cosmogenic nuclides, tephrochronology, 14-C dating

1. Introduction

(U–Th)/He zircon dating has demonstrably high potential for Quaternary volcanic chronostratigraphy, but corrections for uranium decay series (U-series) disequilibrium remain a significant source of uncertainty, especially for protracted crystallization and variable pre-eruptive crystal residence times that are common in many volcanic systems (e.g., Farley et al., 2002). Previously published Late Pleistocene (U–Th)/He zircon ages for La Virgen tephra, which erupted from Las Tres Vírgenes volcano (Baja California), met with controversy because conflicting age constraints exist from historical records and various radiometric dating techniques (Schmitt et al., 2006; Schmitt et al., 2007; Capra et al., 2007). For example, Ives (1962) interpreted that Las Tres Vírgenes was historically active based on a map drawn by the Jesuit missionary Ferdinand Konšćac (Ferdinando Consag) in his narrative of travel along the coast of Baja California during 1746 CE. By contrast, Capra et al. (1998) report an uncalibrated ^{14}C age of ~6500 a BP for charcoal from a distal La Virgen tephra deposit. This age, however, was found to be stratigraphically inconsistent with concordant (U–Th)/He zircon ages for La Virgen tephra (36±6 ka at 2σ uncertainty; Schmitt et al., 2006) and the ^{3}He exposure age for overlying basalt lava (26±8 ka; Hausback and Abrams, 1996).

Because the sample dated by the (U–Th)/He zircon method in Schmitt et al. (2006) was from a different locality than the ^{14}C-dated charcoal sample of Capra

et al. (1998), ambiguity remained whether the ages refer to the same eruption. Earlier (U–Th)/He zircon ages were corrected for disequilibrium by assuming a uniform crystallization age estimated from the peak in the U–Th age distribution for a composite population of La Virgen zircons (Schmitt et al., 2006). This was a simplifying assumption due to lack of better age constraints for zircon aliquots that lacked ion microprobe U–Th crystallization ages.

We subsequently explored combined (U–Th)/He and U–Th dating of single zircon crystals to reduce potential bias for zircon populations with heterogeneous crystallization ages. Here, we report ages for La Virgen zircon determined by this method, including samples from the Capra et al. (1998) charcoal location. We also introduce a refined computational tool for (U–Th)/He disequilibrium corrections that calculates eruption ages and uncertainties for individual analyses, and goodness-of-fit parameters in order to assess age concordancy in crystal populations. Eruption ages for La Virgen tephra sampled at the same site as the previously published ^{14}C charcoal sample are compared to new cosmogenic nuclide exposure ages of lava flows to verify stratigraphic consistency.

2. Geological setting

Volcán Las Tres Vírgenes (Fig. 1) is located within the Gulf of California rift zone, and is part of a volcanic ridge that extends from the eastern coast of Baja California towards active sea-floor spreading centers in the Guaymas basin

84 (Fabriol et al., 1999). Volcanism progressed in a counter-clockwise sense from La
85 Reforma caldera to the E (~1.6 – 1.4 Ma), the Aguajito centers to the NE (~1.2 –
86 0.5 Ma), and the central vent edifices of El Viejo and El Azufre to the N (Demant,
87 1981; Garduno-Monroy et al., 1993; Schmitt et al., 2006). The morphologically
88 dominating and most recent volcanic center is the ~15 km^3 Las Tres Vírgenes
89 volcano (Sawlan, 1986; Capra et al., 1998), which comprises early cone-building
90 effusive deposits, overlain by pyroclastic deposits from a later phase of explosive
91 activity. None of these early deposits are radiometrically dated. Las Tres Vírgenes
92 activity culminated in the deposition of the >1.14 km^3 La Virgen tephra which is
93 dispersed in a ~500 km^2 area to the SW of the volcano (Sawlan, 1986; Hausback
94 and Abrams, 1996; Capra et al., 1998). Because of its volume and the volcanic
95 hazard potential of Plinian eruption columns, La Virgen tephra is a key
96 stratigraphic unit whose eruption age has been targeted by several geochronologic
97 studies, yielding conflicting results between ~6,500 a BP (Capra et al., 1998) and
98 36±6 ka (Schmitt et al., 2006).
99 Younger mafic (basalt to basaltic-andesite) lava flows overlying La Virgen tephra
100 erupted from the flanks of the volcano. They comprise two extensive lobes to the
101 S and SE of Las Tres Vírgenes that are 3.4 km and 2.7 km in length, respectively
102 (Fig. 1). We informally name the southern flow Highway Basalt and the
103 southeastern flow Borrego Camp Basaltic-Andesite. A single ^3He exposure age
104 for the Highway basalt flow of 26 ± 8 ka (Hausback and Abrams, 1996) exists,

but no age constraints are available for the Borrego Camp flow. Three morphologically young domes occur south of Las Tres Vírgenes, and are termed here Las Tres Tortugas. Geothermal surface manifestations underlain by a geothermal reservoir are located at the NE base of the volcano. The reservoir is currently exploited for geothermal electricity generation for the nearby port town of Santa Rosalía (Verma et al., 2006).

3. Materials and Methods

3.1. Sampling and locations

In January 2008, we sampled La Virgen tephra at the same location from which Capra et al. (1998) recovered a single fragment of charcoal for ^{14}C dating. The location is on an elevated terrace near the southern edge of a 1 km broad ephemeral stream channel, ~18 km to the SW of Las Tres Vírgenes volcano. We excavated a 1.2 m deep dig to establish the stratigraphy and to sample pumice (Fig. 2). The base of the section is formed by stream-bed cobbles (layer 1). It is overlain by a 60 cm deposit of poorly sorted subangular to rounded pumice with a maximum diameter of 12 mm (layer 2) and minor sand. Between 60 cm depth and the surface, the deposit consists of sand mixed with rounded pumice (max. diameter 30 mm), and is penetrated by abundant plant roots (layer 3). TV0801 is a composite pumice sample from layer 2, collected within 15 cm of the contact to the underlying cobble bed (layer 1).

126 At another location between the middle and the southern Tres Tortugas dome, we
127 collected a composite pumice sample (TV0807) from a well-sorted deposit of
128 light-colored lapilli (maximum diameter 15 mm). The base of this deposit at a
129 thickness of ~20 cm is not exposed, but it is overlain by a 10 - 15 m section of
130 dark scoriaceous air-fall deposits.
131 For sampling original aa lava flow surfaces, we targeted large blocks or spires
132 (several m^2 in cross section) that lack any indication of post-emplacement
133 movement. The top 5 cm of scoriaceous flow surfaces were removed from the
134 center of these blocks using hammer and chisel. Sampled surfaces were from
135 locations that have unobstructed views of the sky, and lack vegetation, soil or ash
136 cover. Despite care of selecting sample locations based on the criteria outlined
137 above, potentially unrecognized erosion of the aa lava flow surfaces would result
138 in cosmogenic dates being minimum ages. The dated samples (Fig. 1) are from
139 Highway Basalt flow (TV0802), Borrego Camp Basaltic-Andesite flow (TV0811),
140 and the southern Tres Tortugas dome (TV0808).
141
142 3.2. Sample preparation
143 Approximately 1 kg of composite pumice clasts were sieved to >6 mm and
144 ultrasonically washed, which caused separation between pumice that floated and
145 dense rocks such as lithic clasts and sand that sank. We note that this procedure
146 only incompletely removed fine-grained sediment adherent to the pumice surfaces.

147 Pumice was subsequently dried at room temperature, crushed, and sieved to <250
148 μm. One aliquot of the <250 μm fraction was digested in HF, another immersed
149 in heavy liquids (tetrabromethane, diiodomethane) to concentrate zircon. Zircon
150 crystals typically ~100–300 μm long and ~50–100 μm wide were hand-picked
151 from both concentrates under a binocular microscope, and pressed into indium
152 (In) metal with crystal surfaces flush on the surface for ion microprobe analysis
153 without any surface preparation besides ultrasonic cleaning, and coating with a
154 conductive layer of 20 - 30 nm of Au. Subsequent to ion microprobe analysis,
155 grains were extracted from the In with a steel needle, photographed, and packed
156 into platinum (Pt) tubes for He degassing (see below).
157 Surface exposure dating was performed on olivine and pyroxene separated from 3
158 to 5 kg rock sample from the top 5 cm of the hand samples. Olivine and pyroxene
159 were concentrated after crushing and sieving from the 250 to 425 and 425 to 850
160 μm size fractions through magnetic and heavy liquid separation, followed by
161 hand-picking under a binocular microscope. Petrographic thin-sections show that
162 crushing did not significantly reduce crystal sizes. Aliquots of the separates were
163 analyzed for major element compositions by electron microprobe, and found to be
164 >97% free from groundmass. Moreover, additional aliquots as well as bulk
165 groundmass samples were ground to <2 μm powder, digested by acid dissolution,
166 and analyzed by inductively coupled plasma mass spectrometry (ICP-MS) to
167 determine U and Th abundances for radiogenic ^{4}He corrections.

168

169 3.3. U–Th ion microprobe analysis

170 Ion microprobe protocols for U–Th analysis using the CAMECA ims 1270 at
171 UCLA followed those described in Schmitt et al. (2006). In addition to ~25 min
172 spot analyses on unpolished rims (depth resolution 5 μm), grain BH91B10 z20
173 was selected for continuous depth profiling from rim to ~30 μm depth. Accuracies
174 of the relative sensitivity calibration for U/Th and background corrections were
175 monitored by replicate analysis of equilibrium zircon standard AS3 mounted next
176 to the unknowns (1099.1 Ma; Paces and Miller, 1993). The average for AS3
177 analyzed interspersed with the unknowns yielded a unity secular equilibrium ratio
178 for $(^{230}Th)/(^{238}U) = 0.998 \pm 0.010$ (activities denoted in parentheses; MSWD = 2.2;
179 n = 8). Uranium concentrations were estimated from $UO^+/Zr_2O_4^+$ intensity ratios
180 relative to zircon standard 91500 (81.2 ppm U; Wiedenbeck et al., 2004).
181 Crystallization ages were calculated as two-point zircon - melt isochrons using La
182 Virgen tephra whole-rock compositions in Schmitt et al. (2006).

183

184 3.4. (U–Th)/He analysis

185 (U–Th)/He age determinations were carried out at the University of Kansas using
186 laboratory procedures described in Biswas et al. (2007). Zircons were wrapped in
187 Pt foil, heated for 10 minutes at 1290°C and reheated until >99% of the He was
188 extracted from the crystal. All ages were calculated using standard α-ejection

189 corrections using morphometric analyses (Farley et al., 1996). After laser heating,
190 zircons were unwrapped from the Pt foil and dissolved using double-step HF-
191 HNO_3 and HCl pressure-vessel digestion procedures (Krogh, 1973). U, Th, and
192 Sm concentrations were determined by isotope dilution ICP-MS analysis. The
193 laboratory routinely analyzes zircon standards with independently determined
194 ages, and we report averages for Fish Canyon tuff zircons of 27.8 ± 0.8 Ma
195 (RSD% = 7.5%, n = 285) and Durango zircons of 30.2 ± 1.1 Ma (RSD%= 6.8; n =
196 76). From the reproducibility of replicate analyses of these laboratory standard
197 samples we estimate analytical uncertainties of 8% (1σ) for individual zircon (U–
198 Th)/He ages.
199
200 3.5. Surface exposure dating
201 Approximately 0.65-1.50 g samples of the olivine/pyroxene separates of TV0802,
202 TV0808, and TV0811 were weighed, wrapped in Al foil, and loaded into the
203 sample carrousel of the ultrahigh vacuum furnace at the GFZ Potsdam noble gas
204 lab. Noble gases were extracted by stepwise heating at 600, 900, and 1750°C.
205 Active gases were removed in a dry ice trap, two titanium sponge or foil getters,
206 and two SAES (Zr-Al) getters. The noble gases were then trapped at 11K on
207 activated charcoal in a cryogenic adsorber and sequentially released for separate
208 He, Ne, and Ar-Kr-Xe analysis in a VG5400 noble gas mass spectrometer.
209 Corrections for isobaric interferences of $^{40}Ar^{++}$ at m/e=20 and $^{12}C^{16}O^{++}$ at m/e=22

were applied according to Niedermann et al. (1997); a correction for $H_2{}^{18}O^+$ at m/e=20 was not necessary due to the mass resolution of ≥600 of the VG5400. Analytical blanks were 10^{-11}-10^{-10} cm^3 STP for ^{4}He and 0.6-2.2×10^{-12} cm^3 STP for ^{20}Ne depending on extraction temperature, with atmospheric isotopic compositions. This corresponds to 400-4000 atoms ^{3}He and 50,000-170,000 atoms ^{21}Ne.

Before being loaded to the extraction furnace, the TV0802 and TV0811 samples had been crushed in vacuo in order to determine the isotopic composition of He and Ne trapped in fluid inclusions. From TV0808 enough material was available to use a separate aliquot for the crushing extraction. In our manually operated crusher, samples are simply squeezed between two hard metal jaws, which minimizes the possibility for any loss of cosmogenic He. Crusher blanks were ~4×10^{-12} cm^3 STP and 0.5×10^{-12} cm^3 STP for ^{4}He and ^{20}Ne, respectively.

3.6. Correction procedures for combined U–Th and (U–Th)/He dating

Zircon crystallization results in significant disequilibrium in U-series decay chains (e.g., Farley et al., 2002). Deficits in intermediate daughter isotopes (mainly ^{230}Th with a half-life of ~75.7 ka) at the time of eruption will lead to retardation in ^{4}He accumulation compared to a crystal that is in secular equilibrium, and consequently an underestimation of the eruption age. Other longer-lived daughter isotopes that can be fractionated from parental U isotopes

231 are ^{231}Pa (half-life ~32.8 ka) and ^{226}Ra (half-life ~1.6 ka). Disequilibrium in ^{231}Pa
232 and ^{226}Ra, however, has only minor and compensatory effects on (U–Th)/He
233 zircon ages, so that they can be reasonably neglected except for zircons with very
234 young crystallization ages (Farley et al., 2002).
235 If the magma was in secular equilibrium, as is the case of La Virgen tephra
236 (Schmitt et al., 2006), the deficit in ^{230}Th at the time of zircon crystallization can
237 be calculated from the D_{230} parameter (Farley et al., 2002):

238 $$D_{230} = (Th/U)_{zircon}/(Th/U)_{magma} \quad (1)$$

239 which can be approximated from the ratio between Th/U in zircon and whole-rock
240 or matrix glass. The amount of initial U-series disequilibrium in zircon described
241 by D_{230}, however, will diminish due to radioactive ingrowth of ^{230}Th if sufficient
242 time elapses between zircon crystallization and eruption. Crystal residence at
243 elevated temperature or reheating at the time of eruption prevents ^{4}He
244 accumulation in zircon. Thus, constraining the effective D_{230} at the time of
245 eruption ($^{eruption}D_{230}$) is critical for accurate disequilibrium correction of young
246 (U–Th)/He ages.
247 In order to determine $^{eruption}D_{230}$ and to correct (U–Th)/He ages, we developed a
248 Monte Carlo computational routine ("MCHeCalc") that calculates probability
249 density functions for disequilibrium corrected (U–Th)/He ages based on the
250 following input variables: (1) uncorrected (U–Th)/He ages, (2) U–Th
251 crystallization ages, and (3) D_{230} (at the time of crystallization). In the

computation, a (U–Th)/He age is first randomly picked from the Gaussian distribution represented by the equilibrium age and its uncertainty (standard error σ). Then, an associated crystallization age is randomly picked from the measured crystallization age Gaussian distribution as described above. In a third step, each randomly picked (U–Th)/He age is corrected for disequilibrium by calculating $^{eruption}D_{230}$ using the differential equations for n-nuclide decay series (Bateman, 1910) and the corresponding random pick from the crystallization age distribution. Monte Carlo calculations of the eruption age probability density functions comprise 100,000 or 1,000,000 trials per individual analysis. The software is designed to disregard and repeat trials that violate the constraint that eruption must post-date crystallization. The resulting eruption age distributions are usually pseudo-Gaussian with slightly asymmetric standard deviations. A "concordant" eruption age probability density function is calculated from the intersection of all individual eruption age distributions. This "concordant" age distribution is also pseudo-Gaussian and can be represented by its peak age and its asymmetric associated uncertainties. Finally, the program estimates a goodness of fit parameter Q using the regularized gamma function (Press et al., 2002):

$$Q = gammq\ [(n-1)/2,\chi^2/2] \quad (2)$$

where χ^2 is the "chi-square" between the "concordant" eruption age and the individual zircon eruption ages, and n is the number of measurements. A model fit is considered acceptable if $Q \geq 0.001$ (Press et al., 2002).

For testing of our computational routine, we modeled published Rangitawa tephra zircon data of known eruption age (330 ka; Farley et al., 2002) that show crystal residence times between 0 and >380 ka (i.e., secular equilibrium). By reproducing the independently determined 330 ka eruption age of Rangitawa tephra (Farley et al., 2002) to within <2%, we confirmed the reliability of our computational routine (MCHeCalc age: 326±6 ka; n = 15; goodness-of-fit of 0.99). The MCHeCalc program (MCHeCalc.exe) and the Rangitawa test file (Farley.in) is available for download as an electronic appendix.

4. Results

4.1. La Virgen tephra zircon

U–Th zircon rim ages for La Virgen tephra sample TV0801 (Table 1) range between ~34 ka and >380 ka (secular equilibrium). The crystallization age distribution for zircon rim ages of TV0801 extends to younger ages relative to BH91B10 zircon interiors (Schmitt et al., 2006), but rim and interior ages overlap (Fig. 3). Continuous depth profiling of grain BH91B10 z20 (Fig. 4) yielded a rim age of 59^{+22}_{-20} ka (2σ; MSWD = 0.63; 0 - 7.5 μm), whereas the core age averages 157^{+36}_{-34} ka (MSWD = 1.1; 7.5 - 22.5 μm). Conventional ion microprobe spot analyses of the same crystal at a lateral resolution of 20 - 25 μm yielded ages of 129^{+48}_{-40} ka (rim) and 200^{+86}_{-62} ka (core; Fig. 3). The core ages in spot analyses and

depth profiles overlap within uncertainty. Rim spot ages, however, are older than those on unpolished surfaces analyzed during depth profiling. This is likely due to beam overlap onto interior age domains in spot analyses where spatial resolution is limited by lateral beam dimensions.

Approximately one third (five out of 13) of the TV0801 zircon rim analyses yield secular equilibrium ages (Table 1). Secular equilibrium grains are thus nearly twice as abundant in TV0801 compared to previously dated sample BH91B10 with three grains out of 14 in secular equilibrium (Schmitt et al., 2006). Even more striking is the difference between (U–Th)/He ages for the secular equilibrium zircons in both samples: four TV0801 secular equilibrium zircon crystals yielded comparatively old (U–Th)/He ages between ~1 Ma and 22 Ma (Table 1), much older than the remaining ages between ~18 and ~37 ka (prior to correction for disequilibrium; Table 1). This is in contrast to previously dated zircon crystals from BH91B10 that show entirely Late Pleistocene (36±6 ka) (U–Th)/He ages, despite the fact that some of these crystals have Mid Cenozoic to Early Mesozoic crystallization ages. Secular equilibrium crystals in proximal sample BH91B10 thus became completely degassed at the time of eruption, whereas those in distal sample TV0801 preserved pre-eruptive (U–Th)/He ages. The exception is TV0801 z13 with a secular equilibrium U–Th rim age and a Late Pleistocene (U–Th)/He age.

313 Monte Carlo models for TV0801 zircons (disequilibrium-uncorrected average:
314 22.3±5.3 ka) were run using the overall average U–Th age (146±110 ka) or
315 individual U–Th rim ages as estimates for the crystallization age of the entire
316 grain (Fig. 5). In both cases, the disequilibrium-corrected age of grain TV0801
317 z18 is an outlier to older ages, resulting in very low probabilities for the model (Q
318 = 1.4×10^{-7} and 2.8×10^{-7}, respectively). Because zircon age zonation is
319 demonstrably present in La Virgen zircons (Fig. 3), the ~41 ka rim age of TV0801
320 z18 is a minimum for the bulk crystallization age. When re-calculated assuming
321 equilibrium, grain z18 falls in line with the rest of the population, and the
322 goodness of fit improves significantly ($29.1^{+2.2}_{-2.0}$ ka; Q = 0.0012; Fig. 5C).
323 Individually disequilibrium-corrected ages (Table 1) thus yield the best results,
324 with the caveat that potential age zonation could lead to overcorrected (= too old)
325 eruption ages.
326 For sample TV0807, the uncorrected average (U–Th)/He zircon age is 22.5±8.4
327 ka. Disequilibrium correction using individual rim U–Th ages or the average U–
328 Th increases the eruption age estimate, but result in low probabilities of fit
329 because of outlier grain TV0807 z2 (Q = 7×10^{-13} and 3×10^{-6}, respectively).
330 Assuming equilibrium for the bulk of grain TV0807 z2, a much better overall fit
331 is obtained for the individually corrected ages (Fig. 5G). The average age of
332 $30.6^{+2.8}_{-2.4}$ ka (Q = 0.009) is indistinguishable from that of the other locations.

333

334 4.2. Mafic lavas

335 The results of He and Ne analyses of olivine/pyroxene separates from surface
336 mafic lavas are presented in Table 2. According to the crushing extractions of
337 TV0802 and TV0808, the magmatic $^3He/^4He$ ratio in Tres Vírgenes olivine and
338 pyroxene is $(10.15 \pm 0.90)\times10^{-6}$ (weighted mean), or 7.30 ± 0.65 R_A, where R_A is
339 the atmospheric $^3He/^4He$ ratio of 1.39×10^{-6}. We do not consider the result from
340 TV0811, which released an order of magnitude less He than the other two
341 samples during crushing. The cosmogenic ^3He concentrations (^3He_c) shown in
342 Table 3 have been calculated from the stepwise heating data according to

343 $$^3He_c = [(^3He/^4He)_{measured} - (^3He/^4He)_{magmatic}] \times {}^4He_{measured} / R \quad (3)$$

344 and summing up the three heating steps. R is a correction factor proposed by
345 Blard and Farley (2008), who have pointed out that ^3He exposure ages may be
346 underestimated when the possible presence of radiogenic ^4He in the olivine or
347 pyroxene minerals is not taken into account. ^4He is being produced since eruption
348 of the lava by U and Th decay, either in the mafic lava matrix and injected into
349 the phenocrysts or within the phenocrysts. To assess the possible influence of
350 radiogenic ^4He, we have determined U and Th concentrations in both the matrix
351 and the phenocrysts by ICP mass spectrometry at the GFZ Potsdam. The results
352 (Table 4) indicate a ^4He production of $0.02\text{-}0.11\times10^{-8}$ cm^3 STP/g in the
353 phenocrysts during their exposure ages, assuming a stopping distance of α

particles of 20 μm and an average crystal diameter of 350 μm (using equation 2 of Blard and Farley, 2008). This corresponds to 1.8-5.1% corrections to the cosmogenic ^{3}He concentrations, or R factors of 0.949-0.982 (Table 4). As the size of the phenocrysts varies and their shape is not ideally spherical, we assign a conservative 50% uncertainty (i.e., (1-R)/2) to these corrections.

For Ne, the crushing extractions as well as the 600°C and 900°C data showed essentially atmospheric isotopic composition. In a three-isotope plot (not shown), the 1750°C data lie on the mixing line of air and cosmogenic Ne (Schäfer et al., 1999) within uncertainties. Therefore, cosmogenic ^{21}Ne (Table 3) was obtained as the excess over atmospheric abundances and is dominantly determined by the 1750°C step.

To calculate surface exposure ages from the cosmogenic ^{3}He and ^{21}Ne concentrations, the production rates at the sampling location for the respective mineral chemistry have to be known. While the ^{3}He production rate depends only slightly on chemical composition (e.g. Masarik, 2002), the ^{21}Ne production rate varies substantially, in particular with Mg content. In the past, production rates of ^{3}He and ^{21}Ne as obtained by experimental determinations (e.g. Cerling and Craig, 1994; Licciardi et al., 1999) or physically-based model calculations (e.g. Masarik, 2002; Kober et al., 2005) have yielded inconsistent ^{3}He and ^{21}Ne exposure ages (Niedermann et al., 2007; Fenton et al., 2009). Here we use the method of Fenton et al. (2009) to calculate sea level/high latitude production rates (Table 3) based

375 on the major element composition of each sample as determined by microprobe
376 analysis (Table 5). These authors adjusted the model data of Masarik (2002) to the
377 experimental production rate determinations of Poreda and Cerling (1992) and
378 Cerling and Craig (1994) in order to provide consistent ^{3}He and ^{21}Ne exposure
379 ages. Scaling for altitude and latitude was performed according to Stone (2000);
380 the corresponding scaling factors are also shown in Table 3. Corrections for
381 horizon shielding are negligible, and self-shielding of the <5 cm samples was not
382 accounted for as the cosmic-ray neutron flux is expected to be constant in the
383 topmost few centimeters of rock (Masarik and Reedy, 1995). The resulting ^{3}He
384 and ^{21}Ne exposure ages (Table 3) are between ~22 and 42 ka. The 2σ
385 uncertainties are relatively large for ^{21}Ne (~15-90%); however the ^{3}He ages are
386 quite precise, and the ^{3}He and ^{21}Ne ages are consistent for each sample.
387 Systematic uncertainties of production rates and scaling factors are not included
388 in the error limits of the exposure ages. For example, if ^{3}He production rates were
389 higher than assumed here (e.g. Blard et al., 2006), the ages might decrease by
390 ~10%. Likewise, accounting for geomagnetic field variations in the past 22-42 ka
391 would increase production rates and therefore decrease exposure ages by ~2-6%
392 (Masarik et al., 2001) at the latitude of Tres Vírgenes.
393
394 5. Discussion
395 5.1. Combined U–Th and (U–Th)/He zircon geochronology

New and published zircon results for La Virgen tephra indicate the presence of a complex zircon population that includes xenocrysts and late Pleistocene zircons that pre-date the eruption by up to ~200 ka. Depth profiling demonstrates that protracted crystallization can be recorded in a single grain. This has implications for correcting (U–Th)/He ages for disequilibrium because interior crystallization ages are unknown, unless continuous age spectra for individual grains are obtained by depth profiling. This is, however, impractical because of long analysis durations (~10 μm/h sputter rate) that limit efficient sampling. U–Th rim analysis of zircon provides a minimum estimate for the age of the zircon, and allows screening for older grains that are closer to secular equilibrium, thus mitigating the effects of disequilibrium on (U–Th)/He ages.

Our new Monte Carlo computation of (U–Th)/He zircon eruption ages provides a rapid way of assessing the homogeneity of age populations. Data from La Virgen tephra show that (U–Th)/He eruption ages can be overcorrected if the rim age is used as representative for the entire grain, but replicate (U–Th)/He analyses of zircons with a range of rim crystallization ages (or preferentially magmatic xenocrysts in secular equilibrium) allow to identify such grains.

5.2. The age of La Virgen tephra

Based on the combined (U–Th)/He zircon results for proximal and distal La Virgen tephra (locations TV0801 and BH91B10), we recalculate the eruption age

417 at $30.7^{+1.8}_{-1.4}$ ka (n = 14; Q = 0.0014). For this, we used data from Table 1 and those
418 published in Schmitt et al. (2006). Because individual crystallization age
419 constraints were in part lacking for our previous data, we used an average
420 crystallization age (146±110 ka) for the Schmitt et al. (2006) zircon crystals.
421 This age overlaps within uncertainty with the previously reported eruption age for
422 La Virgen tephra (36±6 ka; Schmitt et al., 2006). We also find no difference
423 between the age of the TV0801 tephra at the ^{14}C charcoal site of Capra et al.
424 (1998), and the proximal BH91B10 tephra previously analyzed (Schmitt et al.,
425 2006), indicating that they represent the same eruption. Furthermore, both
426 samples overlap in age with silicic tephra sample TV0807 from the vicinity of the
427 Tres Tortugas domes where it underlies more mafic tephra. The extent of the
428 overlying mafic tephra and its origin remains unconstrained. Based on its
429 comparatively old surface exposure age (42.5±3.8 ka; TV0808), the southernmost
430 dome can be ruled out as the source of the mafic tephra, leaving the middle or the
431 northern dome as potential sources.
432 Our new data rule out the possibility that the sampling sites of Capra et al. (1998)
433 and Schmitt et al. (2006) represent separate eruptions. The ambiguity arising from
434 conflicting (U–Th)/He zircon and ^{14}C ages is further resolved by new surface
435 exposure ages for mafic lavas (TV0802 and TV0811) that support previous
436 cosmogenic dating results (Hausback and Abrams, 1996). Both lavas lack tephra
437 cover, and in the case of the Highway basalt flow are entirely surrounded by La

438 Virgen tephra. The younger exposure ages of both mafic lava flows (^{3}He exposure
439 ages of 25.5±4.4 ka and 22.0±2.5 ka) are stratigraphically consistent with the
440 eruption age for La Virgen tephra, although these ages need to be considered as
441 minimum ages for the emplacement if erosion had occurred. The much younger
442 ^{14}C charcoal age for La Virgen tephra, however, violates the ^{3}He and ^{21}Ne age
443 constraints for the overlying basalt flows.
444 (U–Th)/He zircon ages in sample TV0801 shed additional light on the problem of
445 a conflictingly young ^{14}C charcoal age. Old (U–Th)/He zircon ages of ~1 Ma and
446 ~22 Ma in TV0801 match ages of nearby exposed silicic tuffs from La Reforma
447 caldera and Comondú volcanics, respectively (Sawlan, 1986; Schmitt et al., 2006).
448 Such comparatively old (U–Th)/He zircon ages therefore seem geologically
449 reasonable, and they are reproducible. This argues against partial degassing of
450 zircons during eruption or emplacement of the tephra, and is entirely consistent
451 with a complete lack of re-heating above the closure temperature for He in zircon
452 (~180°C; Reiners et al., 2004) at the time of the La Virgen eruption. We
453 consequently interpret these grains as derived from fluvial reworking of sediment
454 after the La Virgen eruption, and therefore of detrital origin. By contrast,
455 proximally sampled tephra shows no evidence for zircon crystals with old (U–
456 Th)/He ages (Schmitt et al., 2006), and all inherited crystals are completely reset
457 with regard to (U–Th)/He. The presence of detrital zircons in TV0801 thus
458 implies significant reworking of La Virgen tephra at the ^{14}C charcoal site. Field

observations such as poor sorting of the deposit, mixing between sand and pumice, subtle rounding of pumice clasts, and deposition within an abandoned fluvial terrace strongly support this notion. This raises suspicion about the charcoal dated by Capra et al. (1998) of being detrital and unrelated to the eruption of La Virgen tephra. We thus reaffirm our conclusion in Schmitt et al. (2006) to disregard the ^{14}C charcoal date as an eruption age, and emphasize that dated explosive activity at Las Tres Vírgenes volcano is entirely pre-Holocene in age. Holocene summit eruptions as postulated by Sawlan (1986) presently remain an untested hypothesis.

6. Conclusions

Combined U–Th and (U–Th)/He zircon geochronology using single crystal analysis provides concordant and internally consistent constraints for crystallization and eruption ages of Quaternary volcanic systems. Corrections of (U–Th)/He data for U-series disequilibrium are based on rim U–Th ages that are regarded as minimum crystallization ages. Zircon age zonations add uncertainty to disequilibrium corrections, but overcorrection can be identified by poor overlap between individual crystal ages. Because U-series disequilibrium is mitigated by long crystal residence, the recommended strategy is to select the oldest juvenile zircons (or xenocrysts) identified by U–Th rim analysis for (U–Th)/He dating. Disequilibrium-corrected (U–Th)/He zircon dating yields reproducible ages that average $30.7^{+1.8}_{-1.4}$ ka (n = 14; Q = 0.0014), combining crystals from proximal and

480 distal sampling locations. This age is stratigraphically consistent with ^{3}He and
481 ^{21}Ne surface exposure ages of overlying mafic lava flows. Slightly older dome
482 lavas occur south of Las Tres Vírgenes volcano. Undegassed zircons in La Virgen
483 tephra from the location that yielded a ^{14}C-dated charcoal fragment (Capra et al.,
484 1998) are strong indications for detrital contamination. We thus call for
485 disregarding the previously published Holocene ^{14}C age for La Virgen tephra.
486

487 ## 7. Acknowledgements

488 We thank Chris Farrar and Felix Wicke for assistance during field work, Tracy
489 Howe for mineral separation, Roman Kislitsyn for (U–Th)/He analysis, Frank
490 Kyte for electron probe analysis, Heike Rothe for ICP-MS measurements, and
491 Enzio Schnabel for performing the noble gas analyses. Janet C. Harvey is
492 acknowledged for generating the DEM plot. Pierre-Henri Blard is thanked for a
493 helpful review. The ion microprobe facility at UCLA is partly supported by a
494 grant from the Instrumentation and Facilities Program, Division of Earth Sciences,
495 National Science Foundation.
496

497 ## 8. References

498 Bateman, H., 1910. The solution of a system of differential equations occurring in
499 the theory of radio-active transformations. Proceedings of the Cambridge
500 Philosophical Society 15, 423-427.

501 Biswas, S., Coutand, I., Grujic, D., Hager, C., Stockli, D., Grasemann, B., 2007.
502 Exhumation and uplift of the Shillong plateau and its influence on the
503 eastern Himalayas: New constraints from apatite and zircon (U–Th-
504 [Sm])/He and apatite fission track analyses. Tectonics 26(6), TC6013.
505 Blard, P.-H., Farley, K.A., 2008. The influence of radiogenic ^{4}He on cosmogenic
506 ^{3}He determinations in volcanic olivine and pyroxene. Earth and Planetary
507 Science Letters 276(1-2), 20-29.
508 Blard, P.-H., Pik, R., Lavé, J., Bourlès, D., Burnard, P.G., Yokochi, R., Marty, B.,
509 Trusdell, F., 2006. Cosmogenic ^{3}He production rates revisited from
510 evidences of grain size dependent release of matrix-sited helium. Earth
511 and Planetary Science Letters 247, 222-234.
512 Capra, L., Macias, J.L., Espindola, J.M., Siebe, C., 1998. Holocene plinian
513 eruption of La Virgen Volcano, Baja California, Mexico. Journal of
514 Volcanology and Geothermal Research 80(3-4), 239-266.
515 Capra, L., Siebe, C., Macias, J.L., Espindola, J.M., 2007. Comment on: Schmitt,
516 AK et al. (2006): Eruption and magma crystallization ages of Las Tres
517 Vírgenes (Baja California) constrained by combined ^{230}Th/^{238}U and (U–
518 Th)/He dating of zircon [J. Volcanol. Geotherm. Res. 158: 281-295].
519 163(1-4), 98-101.

520 Cerling, T.E., Craig, H., 1994. Cosmogenic ^{3}He production rates from 39°N to
521 46°N Latitude, western USA and France. Geochimica.et Cosmochimica
522 Acta 58(1), 249-255.
523 Demant, A., 1981. Plio-Quaternary volcanism of the Santa Rosalia area, Baja
524 California, Mexico. In: Ortlieb, L., Roldan-Quintana, J. (Eds.), Geology of
525 Northwestern Mexico and Southern Arizona, Field Guides and Papers.
526 U.N.A.M, Inst. Geol., Estación Regional del Noroeste, Mexico City,
527 Mexico D.F., pp. 295–307.
528 Fabriol, H., Delgado-Argote, L.A., Danobeitia, J.J., Cordoba, D., Gonzalez, A.,
529 Garcia-Abdeslem, J., Bartolome, R., Martin-Atienza, B., Frias-Camacho,
530 V., 1999. Backscattering and geophysical features of volcanic ridges
531 offshore Santa Rosalia, Baja California Sur, Gulf of California, Mexico.
532 Journal of Volcanology and Geothermal Research 93(1-2), 75-92.
533 Farley, K.A., Wolf, R.A., Silver, L.T., 1996. The effects of long alpha-stopping
534 distances on (U–Th)/He ages. Geochimica et Cosmochimica Acta 60(21),
535 4223-4229.
536 Farley, K.A., Kohn, B.P., Pillans, B., 2002. The effects of secular disequilibrium
537 on (U–Th)/He systematics and dating of Quaternary volcanic zircon and
538 apatite. Earth and Planetary Science Letters 201(1), 117-125.
539 Fenton, C.R., Niedermann, S., Goethals, M., Schneider, B., Wijbrans, J., 2009.
540 Evaluation of cosmogenic ^{3}He and ^{21}Ne production rates in olivine and

pyroxene from two Pleistocene basalt flows, western Grand Canyon, AZ, USA. Quaternary Geochronology 4, 475-492.

Garduno-Monroy, V.H., Vargas-Ledezma, H., Campos-Enriquez, J.O., 1993. Preliminary geologic studies of Sierra El Aguajito (Baja California, Mexico): a resurgent-type caldera. Journal of Volcanology and Geothermal Research 59(1-2), 47-58.

Hausback, B.P., Abrams, M.J., 1996. Plinian eruption of La Virgen Tephra, Volcan Las Tres Vírgenes, Baja California Sur, Mexico. Eos, Transactions, American Geophysical Union 77(46, Suppl.), 813-814.

Ives, R.L., 1962. Dating of the 1746 eruption of Tres Vírgenes Volcano, Baja California del Sur, Mexico. Geological Society of America Bulletin 73(5), 647-648.

Kober, F., Ivy-Ochs, S., Leya, I., Baur, H., Magna, T., Wieler, R., Kubik, P.W., 2005. In situ cosmogenic ^{10}Be and ^{21}Ne in sanidine and in situ cosmogenic ^{3}He in Fe-Ti-oxide minerals. Earth and Planetary Science Letters 236(1-2), 404-418.

Krogh, T. E., 1973. Low-contamination method for hydrothermal decomposition of zircon and extraction of U and Pb for isotopic age determinations. Geochimica et Cosmochimica Acta 37(3), 485-494.

Licciardi, J.M., Kurz, M.D., Clark, P.U., Brook, E.J., 1999. Calibration of cosmogenic ^{3}He production rates from Holocene lava flows in Oregon,

562 USA, and effects of the Earth's magnetic field. Earth and Planetary
563 Science Letters 172(3-4), 261-271.
564 Masarik, J., 2002. Numerical simulation of in-situ production of cosmogenic
565 nuclides. Geochimica et Cosmochimica Acta 66(15A), A491-A491.
566 Masarik, J., Reedy, R.C., 1995. Terrestrial cosmogenic-nuclide production
567 systematics calculated from numerical simulations. Earth and Planetary
568 Science Letters 136(3-4), 381-395.
569 Masarik, J., Frank, M., Schäfer, J.M., Wieler, R., 2001. Correction of in situ
570 cosmogenic nuclide production rates for geomagnetic field intensity
571 variations during the past 800,000 years. Geochimica et Cosmochimica
572 Acta 65, 2995-3003.
573 Niedermann, S., Bach, W., Erzinger, J., 1997. Noble gas evidence for a lower
574 mantle component in MORBs from the southern East Pacific Rise:
575 Decoupling of helium and neon isotope systematics. Geochimica et
576 Cosmochimica Acta 61(13), 2697-2715.
577 Niedermann, S., Schäfer, J.M., Wieler, R., Naumann, R., 2007. The production
578 rate of cosmogenic ^{38}Ar from calcium in terrestrial pyroxene. Earth and
579 Planetary Science Letters 257(3-4), 596-608.
580 Paces, J.B., Miller, J.D., Jr., 1993. Precise U-Pb ages of Duluth Complex and
581 related mafic intrusions, northeastern Minnesota; geochronological
582 insights to physical, petrogenetic, paleomagnetic, and tectonomagnetic

processes associated with the 1.1 Ga Midcontinent Rift System. Journal of Geophysical Research, B, Solid Earth and Planets 98(8), 13,997-14,013.

Poreda, R.J., Cerling, T.E., 1992. Cosmogenic neon in recent lavas from the western United-States. Geophysical Research Letters 19(18), 1863-1866.

Press, W.H., Teukolsky, S.A., Vetterling, W.T., Flannery, B.P., 2002. Numerical Recipes: The Art of Scientific Computing. Cambridge University Press, New York.

Reiners, P. W., Spell, T.L., Nicolescu, S., Zanetti, K.A., 2004. Zircon (U–Th)/He thermochronometry: He diffusion and comparisons with $^{40}Ar/^{39}Ar$ dating. Geochimica et Cosmochimica Acta 68(8), 1857-1887.

Sawlan, M.G., 1986. Petrogenesis of Late Cenozoic volcanic rocks from Baja California Sur, Mexico. Doctoral, University of California.

Schäfer, J.M., Ivy-Ochs, S., Wieler, R., Leya, J., Baur, H., Denton, G. H., Schlüchter, C., 1999. Cosmogenic noble gas studies in the oldest landscape on earth: surface exposure ages of the Dry Valleys, Antarctica. Earth and Planetary Science Letters 167(3-4), 215-226.

Schmitt, A.K., Stockli, D.F., Hausback, B.P., 2006. Eruption and magma crystallization ages of Las Tres Vírgenes (Baja California) constrained by combined $^{230}Th/^{238}U$ and (U–Th)/He dating of zircon. Journal of Volcanology and Geothermal Research 158(3-4), 281-295.

603 Schmitt, A.K., Stockli, D.F., Hausback, B.P., 2007. Reply to comment by: Lucia
604 Capra, Claus Siebe, Jose Luis Macias, and Juan Manuel Espindola.
605 Journal of Volcanology and Geothermal Research 163(1-4), 102-103.
606 Stone, J. O., 2000. Air pressure and cosmogenic isotope production. Journal of
607 Geophysical Research, B, Solid Earth and Planets 105(B10), 23753-23759.
608 Verma, S.P., Pandarinath, K., Santoyo, E., Gonzalez-Partida, E., Torres-Alvarado,
609 I. S., Tello-Hinojosa, E., 2006. Fluid chemistry and temperatures prior to
610 exploitation at the Las Tres Vírgenes geothermal field, Mexico.
611 Geothermics 35(2), 156-180.
612 Wiedenbeck, M., Hanchar, J.M., Peck, W.H., Sylvester, P., Valley, J.,
613 Whitehouse, M., Kronz, A., Morishita, Y., Nasdala, L., Fiebig, J., Franchi,
614 I., Girard, J.P., Greenwood, R.C., Hinton, R., Kita, N., Mason, P.R.D.,
615 Norman, M., Ogasawara, M., Piccoli, P.M., Rhede, D., Satoh, H., Schulz-
616 Dobrick, B., Skar, O., Spicuzza, M.J., Terada, K., Tindle, A., Togashi, S.,
617 Vennemann, T., Xie, Q., Zheng, Y.F., 2004. Further characterisation of
618 the 91500 zircon crystal. Geostandards and Geoanalytical Research 28(1),
619 9-39.
620
621 9. Figure legends and tables

622 Fig. 1: Sketch map of Las Tres Vírgenes lava flows and La Virgen tephra overlain
623 on digital elevation model (Aster Global DEM at 30 m resolution). Sample
624 locations are indicated.
625
626 Fig. 2: Stratigraphic columns for sample locations (A) TV0801 (equivalent to
627 TV9564 in Capra et al. 1998 and 2007) and (B) BH91B10 (Schmitt et al., 2006).
628 Boxes indicate horizons from which composite pumice samples for (U–Th)/He
629 zircon dating were collected. The charcoal dated by Capra et al. (1998) was
630 recovered near the base of layer 2.
631
632 Fig. 3: U–Th zircon crystallization ages and U/Th in zircon for TV0801 (distal La
633 Virgen) and TV0807 (tephra near Tres Tortugas) in comparison to published data
634 BH91B10 (Schmitt et al., 2006).
635
636 Fig. 4: U–Th zircon crystallization ages for grain BH91B10 z20 in spot analysis
637 of crystal interiors (A), and depth profiling (B). Cathodoluminescence image of
638 grain interior exposed by grinding and polishing (C), and original crystal surface
639 in backscatter electron imaging (D). Locations of core and rim, as well as depth
640 profiling analysis spots are indicated.
641

642 Fig. 5: (U–Th)/He ages and average age relative probability curves for TV0801
643 (A-D) and TV0807 (E-H). (U–Th)/He ages uncorrected for disequilibrium with
644 weighted averages and values for mean square of weighted deviates (MSWD).
645 Uncorrected data in A and E show high MSWD values, suggesting scatter due to
646 disequilibrium in young zircons. Disequilibrium-corrected (U–Th)/He ages using
647 an average crystallization age of 146±110 ka from U–Th zircon analysis (B and
648 F) still yields poor model fits (Q <0.001) for both samples. Individually
649 disequilibrium-corrected (U–Th)/He ages using U–Th rim ages (closed symbols)
650 yield acceptable fits (Q >0.001) when outliers TV0801 z18 and TV0807 z2 are
651 adjusted assuming equilibrium (open symbols). This is supported by plotting U–
652 Th zircon crystallization vs. individually disequilibrium-corrected (U–Th)/He
653 eruption ages (D and H), where all zircon crystals satisfy the condition that
654 eruption must postdate crystallization (i.e., the data plot above the 1 : 1 line).
655 Otherwise, applying a disequilibrium correction based on the rim U–Th
656 crystallization would result in overcorrection of crystals TV0801 z6 and TV0807
657 z2 whose interior may be much older (see also Fig. 4).
658
659 Table 1: Combined U–Th and (U–Th)/He zircon dating results.
660

661 Table 2: Results of He and Ne analyses in olivine/pyroxene separates from basalt
662 to basaltic-andesite surface rocks. Noble gas concentrations are in units of cm^3
663 STP/g, error limits are 2σ.
664
665 Table 3: Concentrations of cosmogenic ^3He and ^{21}Ne, adopted ^3He and ^{21}Ne
666 production rate values (P_3 and P_{21}) for sea level and high latitude (as calculated
667 from elemental composition according to Fenton et al., 2009), altitude/latitude
668 scaling factors (Stone, 2000), and resulting ^3He and ^{21}Ne exposure ages (T_3 and
669 T_{21}). Cosmogenic ^3He concentrations have been corrected for radiogenic ^4He
670 (Blard and Farley, 2008) using R factors shown in Table 4. Asymmetric
671 uncertainties for $^{21}Ne_c$ are caused by atmosphere-like $^{21}Ne/^{20}Ne$ ratios in the
672 600°C and 900°C steps (Table 2), for which only the fraction of the uncertainty
673 range reaching above atmospheric was taken into account as lower-than-
674 atmospheric $^{21}Ne/^{20}Ne$ is physically unreasonable.
675
676 Table 4: Concentrations of Th and U (ppm) in the mafic matrix and in the mineral
677 separates of the investigated surface samples, as determined by ICP mass
678 spectrometry. R factors (Blard and Farley, 2008) were calculated assuming a
679 stopping distance of α particles of 20 μm and an average crystal diameter of 350
680 μm, and were assigned a conservative uncertainty of (1-R)/2**.**
681

682 Table 5: Concentrations of major elements and olivine and pyroxene mineral
683 fractions (all in wt. %) in the investigated mineral separates, as determined by
684 microprobe analysis and used for calculation of ^{3}He and ^{21}Ne production rates
685 after Fenton et al. (2009).
686
687

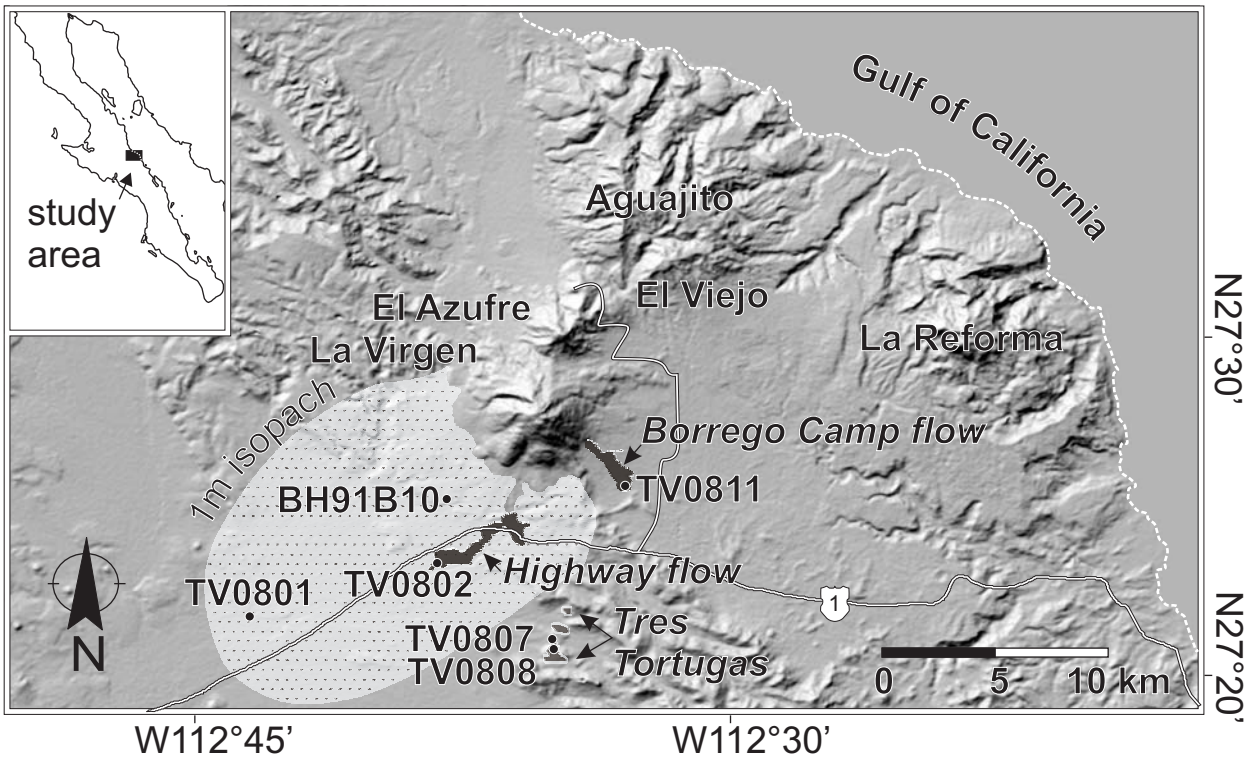

Fig. 1: Schmitt et al., Tres Virgenes

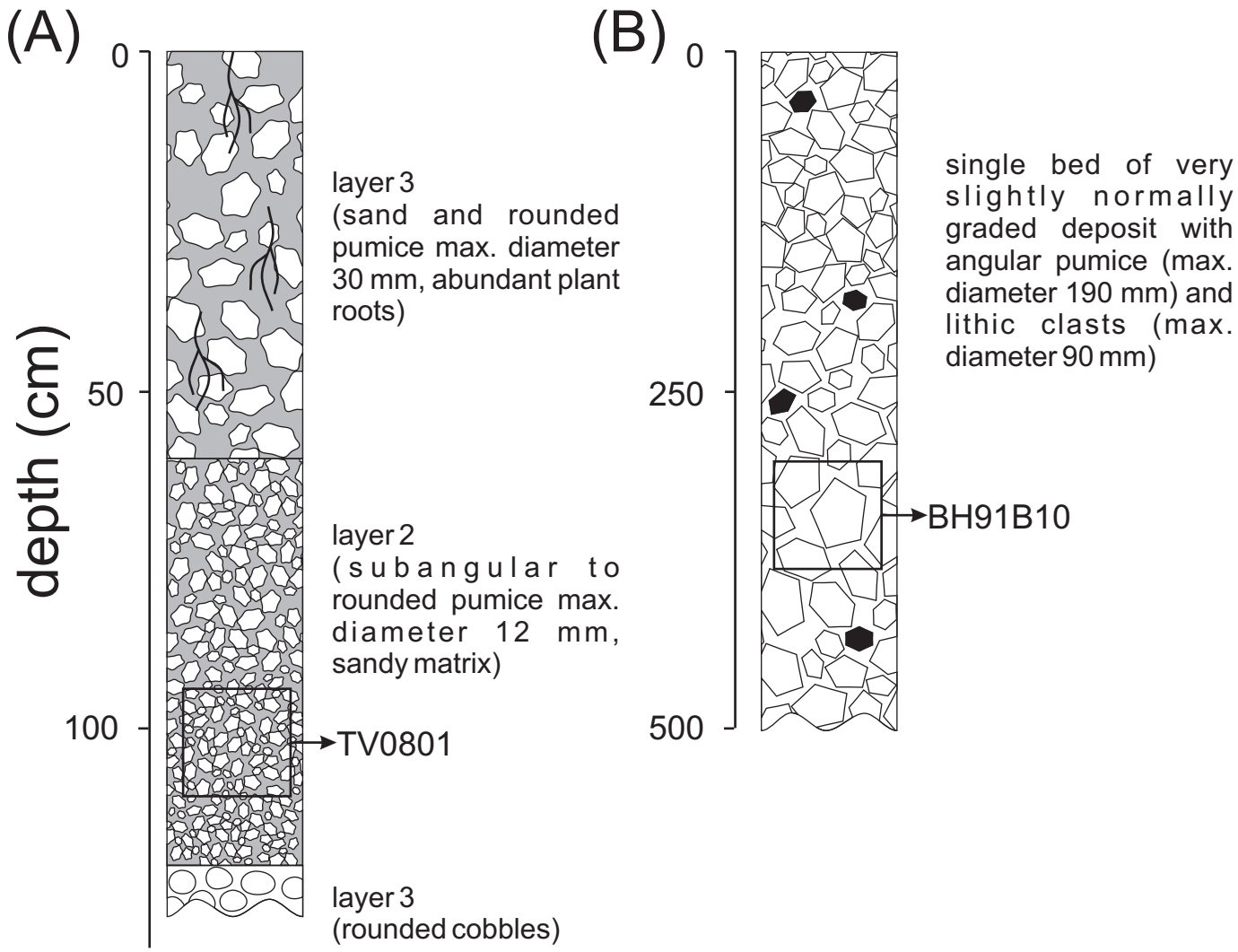

Fig. 2: Schmitt et al., Tres Virgenes

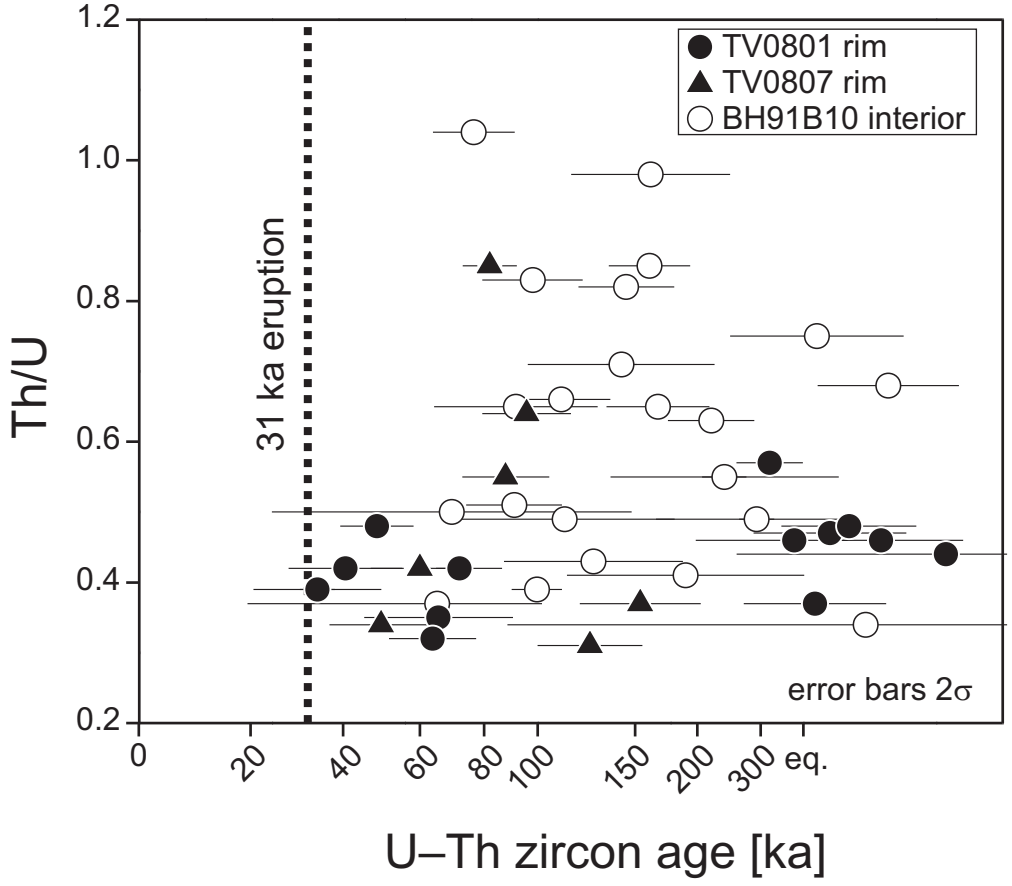
TV0801 rim
TV0807 rim
BH91B10 interior
31 ka eruption
error bars 2σ
Th/U
1.2
1.0
0.8
0.6
0.4
0.2
0
20
40
60
80
100
150
200
300
eq.
U–Th zircon age [ka]

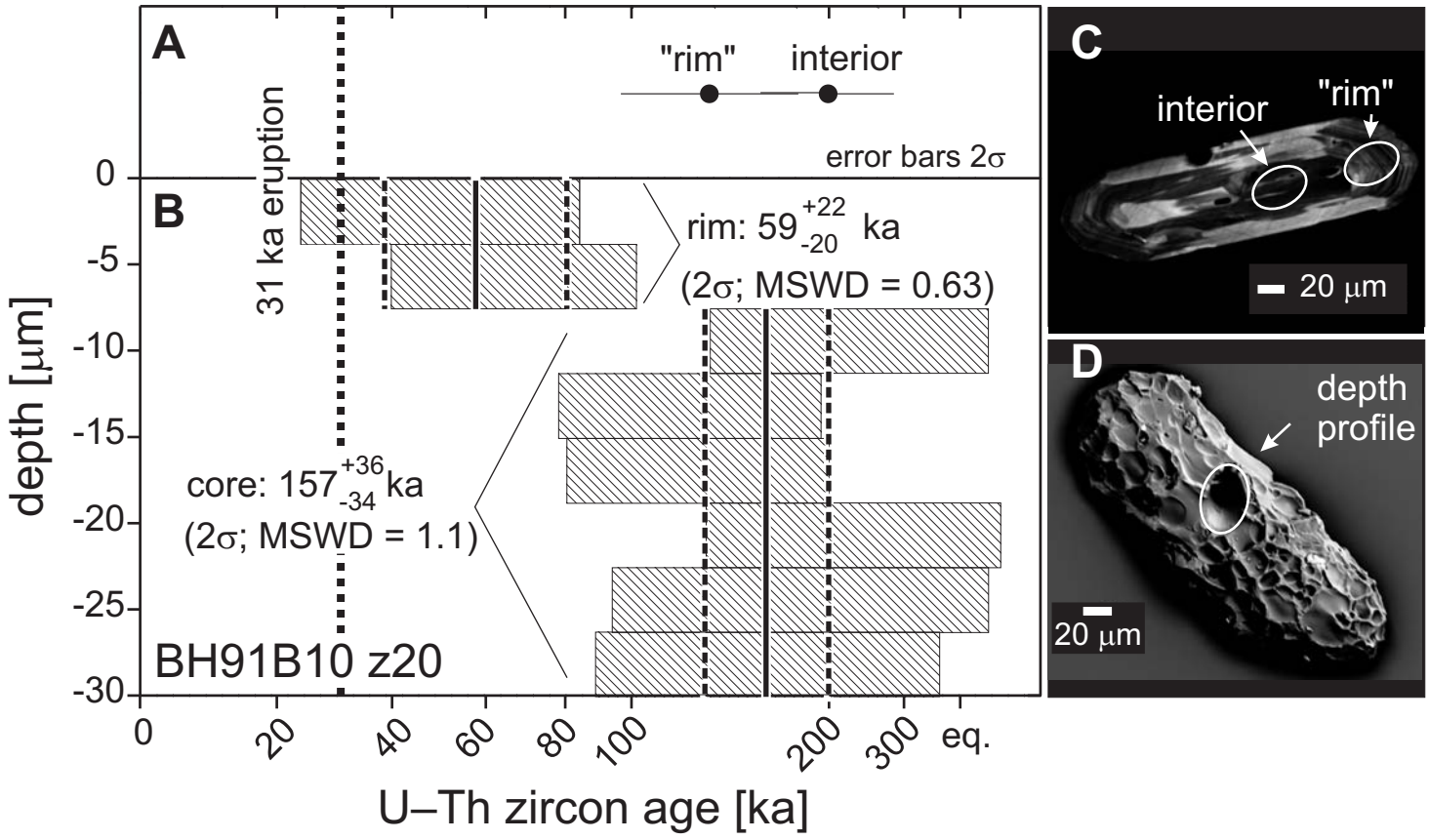
A
"rim"
interior
error bars 2σ
31 ka eruption
B
rim: 59 +22 -20 ka
(2σ; MSWD = 0.63)
core: 157 +36 -34 ka
(2σ; MSWD = 1.1)
BH91B10 z20
depth [μm]
0
-5
-10
-15
-20
-25
-30
0
20
40
60
80
100
200
300
eq.
U–Th zircon age [ka]
C
interior
"rim"
20 μm
D
depth
profile
20 μm

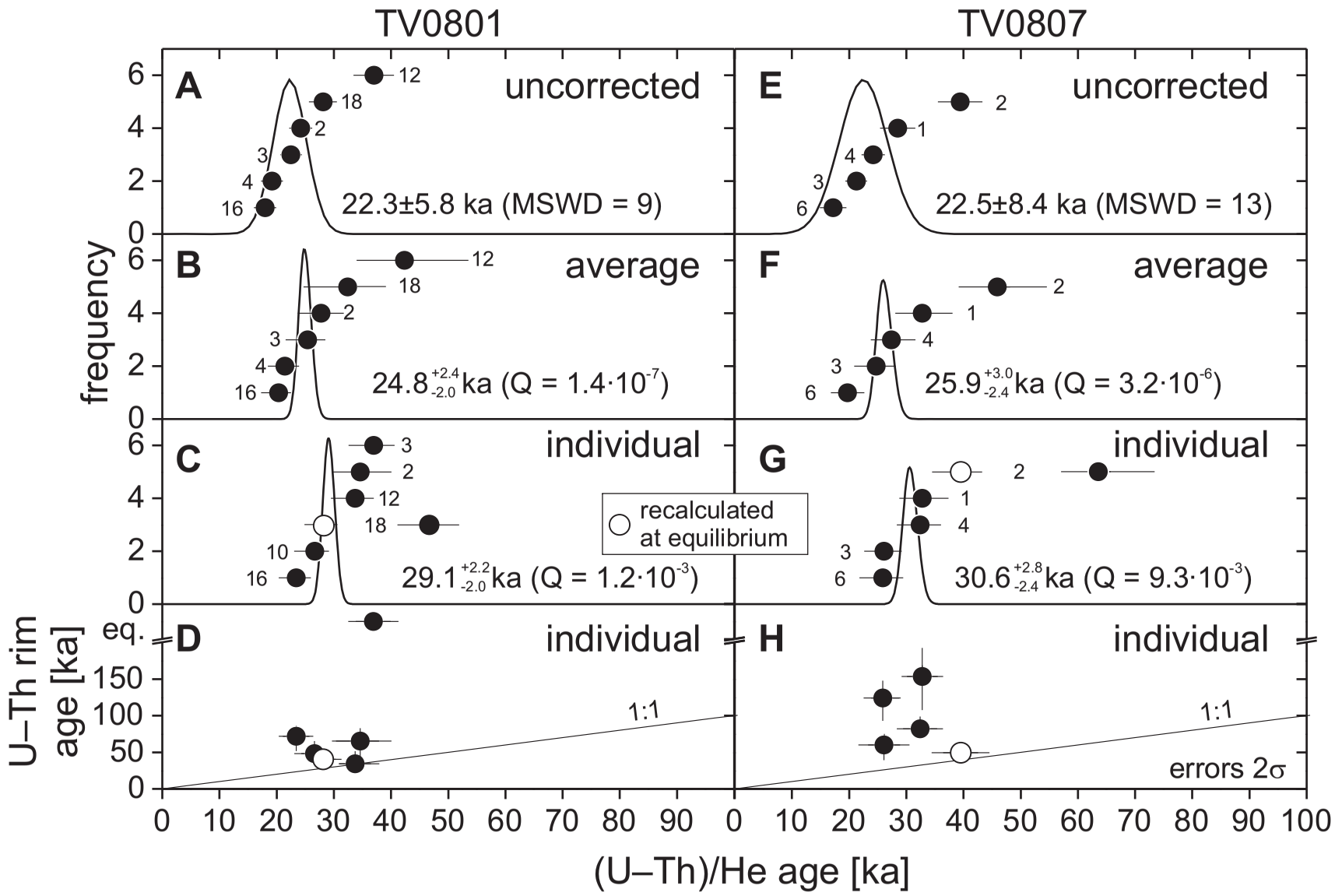
TV0801
TV0807
A
uncorrected
22.3±5.8 ka (MSWD = 9)
E
uncorrected
22.5±8.4 ka (MSWD = 13)
B
average
24.8 +2.4 -2.0 ka (Q = 1.4·10-7)
F
average
25.9 +3.0 -2.4 ka (Q = 3.2·10-6)
C
individual
29.1 +2.2 -2.0 ka (Q = 1.2·10-3)
G
individual
30.6 +2.8 -2.4 ka (Q = 9.3·10-3)
recalculated at equilibrium
D
individual
H
individual
1:1
errors 2σ
frequency
U–Th rim age [ka]
eq.
(U–Th)/He age [ka]

Table 1: U-Th and (U-Th)/He zircon results (all errors 2σ)

	$(^{238}U)/(^{232}Th)$		$(^{230}Th)/(^{232}Th)$		U-Th age			U	Th	D_{230}	He	Ft	equilibrium (U-Th)/He age		disequilibrium (U-Th)/He age			remarks
zircon					ka			ppm	ppm		nmol/g		ka		ka			
		±		±		+	-							±		+	-	
TV0801eruption age: 29.1 +2.2/-2.0 ka (Q = 0.0012)																		
z1	6.94	1.14	8.18	1.55	∞	∞	∞	279	130	n.a.	n.a.	n.a.	n.a.	n.a.	n.a.	n.a.	n.a.	
z2	8.63	0.19	4.48	1.22	65	38	28	95.1	61.4	0.23	0.0109	0.77	24.2	3.9	34.6	8.5	6.6	a
z3	7.77	0.09	2.88	0.67	34	16	14	95.0	87.5	0.32	0.0112	0.80	22.5	3.6	33.7	5.6	5.6	a
z4	6.39	0.20	2.98	0.45	48	16	14	127	128	0.35	0.0116	0.71	19.2	3.1	26.6	4.6	4.7	a
z5	8.28	0.14	8.40	1.11	∞	∞	∞	72.8	31.7	0.15	7.03	0.77	21,100	3,400	*	*	*	b
z11	5.34	0.12	5.11	0.32	325	∞	103	329	240	0.25	33.3	0.72	22,400	3,600	*	*	*	b
z12	9.38	0.28	4.74	0.83	64	22	18	162	55.9	n.a.	n.a.	n.a.	n.a.	n.a.	n.a.	n.a.	n.a.	
z13	6.65	0.07	7.29	0.98	∞	∞	∞	80.8	41.2	0.18	0.0156	0.87	37.0	5.9	*	*	*	c
z14	6.48	0.08	6.68	0.89	∞	∞	∞	122	60	0.17	0.627	0.78	1,100	180	*	*	*	b
z15	6.56	0.07	6.47	0.94	466	∞	282	184.5	91.2	n.a.	n.a.	n.a.	n.a.	n.a.	n.a.	n.a.	n.a.	
z16	7.19	0.09	4.02	0.78	72	31	24	123	114	0.32	0.0111	0.77	18.0	2.9	23.4	4.6	4.0	a
z17	6.29	0.08	6.64	0.77	∞	∞	∞	53.9	26.5	0.17	0.263	0.85	950	160	*	*	*	b
z18	7.30	0.35	3.01	0.78	41	22	18	90.1	48.1	0.19	0.0126	0.82	28.1	4.5	46.7	8.2	7.4	c
TV0807 eruption age: 30.6 +2.8/-2.4 ka (Q = 0.0093)																		
z1	8.16	0.24	6.41	0.95	153	90	49	145	88.9	0.21	0.0209	0.82	28.5	4.6	32.8	7.2	5.4	a
z2	8.83	0.36	3.90	0.70	49	17	15	147	74.9	0.18	0.0278	0.80	39.4	6.3	63.6	14.4	8.8	c
z3	9.93	0.19	7.08	1.07	124	52	35	79.4	42.9	0.19	0.00816	0.79	21.3	3.4	25.9	5.7	4.2	a
z4	3.58	0.11	2.40	0.17	82	18	15	140	98.9	0.25	0.0158	0.74	24.2	3.9	32.4	5.9	5.4	a
z6	7.25	0.14	3.69	0.91	60	32	25	172	94.4	0.19	0.0154	0.86	17.2	2.7	26.1	5.6	6.0	a
z7	4.77	0.08	3.23	0.38	96	32	25	451	306	n.a.	n.a.	n.a.	n.a.	n.a.	n.a.	n.a.	n.a.	
z8	5.48	0.09	3.50	0.45	88	29	23	289	171	n.a.	n.a.	n.a.	n.a.	n.a.	n.a.	n.a.	n.a.	
BH91B10 z2 depth profiling results																		
0-3.8	2.26	0.08	3.05	0.93	49	35	26	139	69.1									
3.8-7.5	2.26	0.03	3.53	0.78	66	34	26	161	80.5									
7.5-11.3	1.89	0.05	4.83	0.70	218	∞	89	191	114									
11.3-15.0	1.72	0.02	3.64	0.59	119	68	42	252	165									
15.0-18.8	1.64	0.02	3.54	0.56	124	74	44	291	200									
18.8-22.5	1.61	0.02	4.15	0.62	221	∞	95	306	214									
22.5-26.3	1.77	0.01	4.29	0.89	177	∞	83	272	173									
26.3-30	1.89	0.02	4.42	0.90	159	254	70	240	143									
"rim"	1.27	0.03	2.86	0.29	129	55	37	318	282									
"core"	1.42	0.03	3.59	0.28	200	116	55	332	264									

Sample locations (WGS-84): TV0801 = N27°22'05", W112°43'50"; TV0807 = N27°21'51", W112°35'02"; BH91B10 = N27°25'42", W112°37'43"
∞ secular equilibrium; n.a. = not analyzed; * = no correction applied (secular equilibrium)
U-Th age from slope through zircon and whole-rock (Schmitt et al., 2006) composition
parentheses denote activities; $D_{230} = [^{232}Th/^{238}U]_{zircon}/ [^{232}Th/^{238}U]_{whole\text{-}rock}$; Ft = alpha particle ejection correction parameter
decay constants used: λ230: $9.1577 \cdot 10^{-6}$ a^{-1}; λ232: $4.9475 \cdot 10^{-11}$ a^{-1}; λ238: $1.55125 \cdot 10^{-10}$ $a^{-1;}$ λ226 = $4.332 \cdot 10^{-4}$ a^{-1}
zircon U-series analyses by ion microprobe
zircon(U-Th)/He analysis by Inductively coupled mass spectrometry (U, Th), and quadrupole mass spectrometry (He)
a = disequilibrium corrected age used for weighted average
b = excluded from weighted average (detrital)
c = equilibrium age used for weighted average

Table 2. Results of He and Ne analyses in olivine/pyroxene separates from basaltic surface rocks. Noble gas concentrations are in units of cm^3 STP/g, error limits are 2σ.

Sample Weight	T °C	^4He 10^{-8}	^{20}Ne 10^{-12}	$^3He/^4He$ 10^{-6}	$^{22}Ne/^{20}Ne$ 10^{-2}	$^{21}Ne/^{20}Ne$ 10^{-2}
TV0802	600	0.0350	112.2	17.5	10.18	0.294
0.98608 g		±0.0019	±5.7	±7.0	±0.13	±0.014
	900	0.1495	90.7	67.6	10.23	0.300
		±0.0075	±4.7	±6.7	±0.12	±0.014
	1750	1.450	37.5	12.00	10.35	0.426
		±0.073	±2.1	±0.64	±0.19	±0.018
	Total	1.635	240.4	17.20	10.23	0.317
		±0.073	±7.7	±0.91	±0.08	±0.009
1.07908 g	crushed	0.639	137.1	10.4	10.219	0.2980
		±0.032	±7.1	±1.1	±0.069	±0.0083
TV0808	600	0.00673	24.0	16	10.20	0.298
1.49926 g		±0.00051	±1.3	±13	±0.18	±0.019
	900	0.1040	210	170	10.078	0.2941
		±0.0052	±11	±12	±0.049	±0.0063
	1750	0.235	68.3	25.6	10.35	0.375
		±0.012	±3.5	±3.7	±0.10	±0.011
	Total	0.346	302	68.9	10.149	0.3127
		±0.013	±12	±4.9	±0.043	±0.0053
1.00896 g	crushed	0.229	223	9.5	10.183	0.294
		±0.012	±12	±1.7	±0.048	±0.010
TV0811	600	0.0753	129.3	46.7	10.18	0.296
0.65236 g		±0.0042	±6.8	±9.7	±0.11	±0.015
	900	0.0528	64.6	132	10.26	0.295
		±0.0030	±3.7	±13	±0.10	±0.018
	1750	0.0428	116.3	27.6	10.30	0.322
		±0.0069	±6.2	±6.2	±0.11	±0.016
	Total	0.1709	310.2	68.3	10.242	0.306
		±0.0086	±9.9	±6.4	±0.065	±0.009
0.65966 g	crushed	0.0206	305	4.8	10.124	0.296
		±0.0019	±16	±3.8	±0.090	±0.013

Sample locations (WGS-84 datum): TV0802 = N27°24'11", W112°38'07", 342 m elevation; TV0808 = N27°21'33", W112°35'11", 503 m elevation; TV0811 = N27°26'04", W112°33'03", 412 m elevation.

Table 3. Concentrations of cosmogenic ^{3}He and ^{21}Ne, adopted ^{3}He and ^{21}Ne production rate values (P_3 and P_{21}) for sea level and high latitude (as calculated from elemental composition according to Fenton et al., 2009), altitude/latitude scaling factors (Stone, 2000), and resulting ^{3}He and ^{21}Ne exposure ages (T_3 and T_{21}). Cosmogenic ^{3}He concentrations have been corrected for radiogenic ^{4}He (Blard and Farley, 2008) using R factors shown in Table 4. Asymmetric uncertainties for $^{21}Ne_c$ are caused by atmosphere-like $^{21}Ne/^{20}Ne$ ratios in the 600°C and 900°C steps (Table 2), for which only the fraction of the uncertainty range reaching above atmospheric was taken into account as lower-than-atmospheric $^{21}Ne/^{20}Ne$ is physically unreasonable.

Sample	$^{3}He_c$	$^{21}Ne_c$	P_3	P_{21}	scaling factor	T_3	T_{21}
	10^6 atoms/g		*at g^{-1} a^{-1}*			*ka*	
TV0802	3.16±0.54	$1.41^{+0.54}_{-0.21}$	119.5	44.7	1.037	25.5±4.4	$30.4^{+11.6}_{-5.3}$
TV0808	5.75±0.52	$1.46^{+0.35}_{-0.22}$	115.5	30.3	1.172	42.5±3.8	$41.1^{+9.9}_{-6.2}$
TV0811	2.78±0.32	$0.83^{+0.79}_{-0.51}$	115.7	27.5	1.095	22.0±2.5	28^{+26}_{-17}

Table 4. Concentrations of Th and U (ppm) in the mafic matrix and in the mineral separates of the investigated surface samples, as determined by ICP mass spectrometry. R factors (Blard and Farley, 2008) were calculated assuming a stopping distance of α particles of 20 µm and an average crystal diameter of 350 µm, and were assigned a conservative uncertainty of (1-R)/2**.**

Sample	Matrix		Phenocrysts		R
	Th	U	Th	U	
TV0802	0.67	0.29	0.05	0.02	0.982 ± 0.009
TV0808	2.3	0.8	0.14	0.07	0.949 ± 0.026
TV0811	2.0	0.6	0.11	0.04	0.960 ± 0.020

Table 5. Concentrations of major elements and olivine and pyroxene mineral fractions (all in wt. %) in the investigated mineral separates, as determined by microprobe analysis and used for calculation of ^{3}He and ^{21}Ne production rates after Fenton et al. (2009)**.**

Sample	O	Na	Mg	Al	Si	Ca	Ti	Fe	ol	px
TV0802	42.7	0.04	25.3	0.32	19.2	2.13	0.10	10.03	87	13
TV0808	42.7	0.17	14.5	0.88	22.4	10.83	0.25	8.02	30	70
TV0811	43.4	0.18	12.0	1.02	24.4	10.35	0.35	8.03	3	97